Activated carbon derived from tree bark biomass with promising material properties for supercapacitors

Damilola Momodu, Moshawe Madito, Farshad Barzegar, Abdulhakeem Bello, Abubakar Khaleed, Okikiola Olaniyan, Julien Dangbegnon and Ncholu Manyala*

Department of Physics, Institute of Applied Materials, SARCHI Chair in Carbon Technology and Materials, University of Pretoria, Pretoria 0028, South Africa.

*Corresponding author's email: ncholu.manyala@up.ac.za, Tel.: +(27)12 420 3549; Fax: +(27)12 420 2516

Graphical abstract:

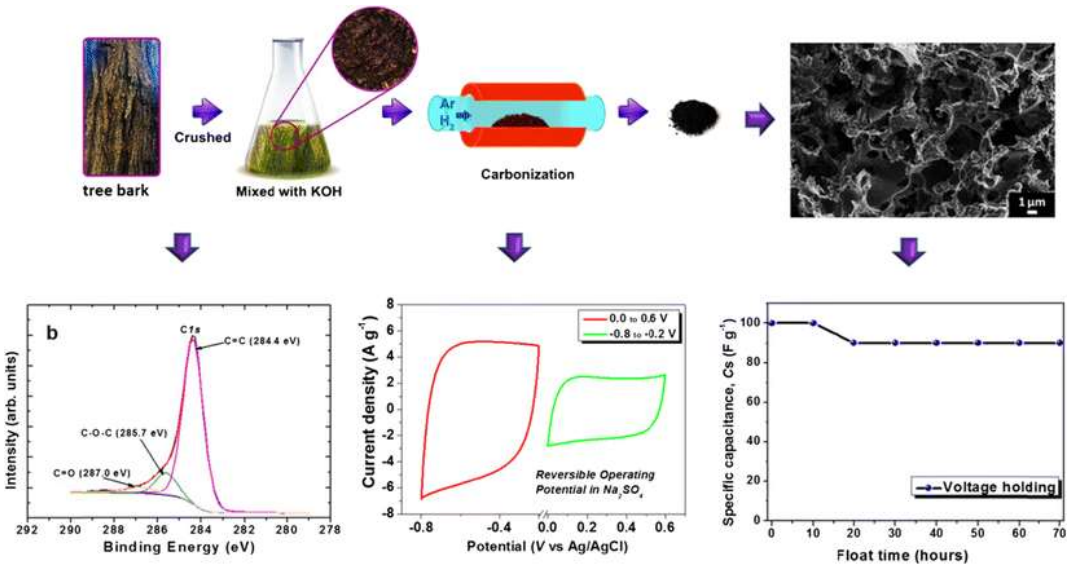

ABSTRACT

Activated carbon from tree bark (ACB) has been synthesized by a facile and environmentally friendly activation and carbonization process at different temperatures (600, 700, and 800 °C) using potassium hydroxide (KOH) pellets as an activation agent with different mass loading. The physicochemical and microstructural characteristics of the as-obtained material revealed interconnected micro/mesoporous architecture with increasing trend in specific surface area (SSA) as carbonization temperatures rises. The SSA values of up to 1018 $m^2 g^{-1}$ and a high pore volume of 0.67 $cm^3 g^{-1}$ were obtained. The potential of the ACB material as suitable supercapacitor electrode was investigated in both a three and two electrode configuration in different neutral aqueous electrolytes. The electrodes exhibited EDLC behaviour in all electrolytes with the Na_2SO_4 electrolyte working reversibly in both the negative (-0.80 V to -0.20 V) and positive (0.0 V to 0.6 V) operating potentials. A specific capacitance (C_S) of up to 191 F g^{-1} at a current density of 1 A g^{-1} was obtained for the optimized ACB electrode material in 1 M Na_2SO_4 electrolyte. A symmetric device fabricated exhibited specific C_S of 114 F g^{-1} at 0.3 A g^{-1} and excellent stability with a coulombic efficiency of a 100% after 5000 constant charge-discharge cycles at 5.0 A g^{-1} and a low capacitance loss for a floating time of 70 h.

Keywords: activated carbon, tree bark, biomass waste, supercapacitor, neutral electrolyte

INTRODUCTION

The need to ensure continuous available and affordable energy for human use in the future has become one of the major concerns of both developed and developing economies today. The use of fossil fuels amongst others has been found to be unsustainable in the long run especially with the major threat to life's existence through global warming as a result of green-house gas emissions [1]. The negative impact on the environment has pushed for research activities into new alternative energy sources which are clean, dependable and safe [2]. A major solution to this problem has been proposed by extensively focusing on major research into renewable energy sources (sun, wind etc.) which are limitless and sustainable. However, the adoption of any renewable energy source largely depends on the quality and ease of accessibility when it is needed [3]. Thus, the major factor related to their exploration can only be solved by adopting efficient energy storage (ES) system mainly based on electrical energy.

Electrochemical capacitors (ECs) are high power storage devices with the ability to be charged and discharge fully in a short period of time. Their high power characteristics coupled with long cycle life has made them useful for a wide range of applications ranging from commercial portable electronic devices, transportation and industrial use [4–7].

Li-ion batteries are also another common example of ES devices which have been in existence much longer and are widely adopted in most storage components. They unfortunately seem to be losing much recognition due to their limitation (such as slow charge-discharge characteristics, limited cycling stability) in high power requirements for emerging advanced technological applications [8]. On the other hand, batteries and their hybrid counterparts generally possess a higher specific energy than ECs and are mostly used

together in an attempt to balance their individual deficiency in power and energy whilst improving their life time [9].

The electrode material plays a key role in determining the device properties of most ES devices including ECs. The electrode material determines to a large extent the mechanism of charge storage of the EC device. Based on the charge storage mechanism, ECs also known as Supercapacitors (SCs) can be classified into two groups namely; the electric double layer capacitors (EDLCs) and Redox capacitors (RCs). EDLCs work purely by electrostatic charge separation at the electrolyte-electrode interface while RCs depend on fast redox processes involving the transfer of charges between the electrode/electrolyte interfaces [10, 11].

Activated carbon (AC) is the oldest and most common material adopted in the design and fabrication of commercial EDLCs. Its chemical stability, low synthesis cost, high surface area and good electrical conductivity available for electro-adsorption and transport of ions to inner pore sites makes ACs attractive for SC applications. Since the charge storage is generally electrostatic, the charge-discharge process involves no active mass transport across the electrode-electrolyte interface and this accounts for the high cycling stability in EDLCs [12]. The main synthesis routes to produce ACs are via the physical and chemical activation of carbon-containing precursors. Chemical activation is preferred to physical activation due to the ability to actively tune and control the material properties towards obtaining the ultimate material performance for EDLCs application [12, 13]. KOH is chosen as a better activating agent compared to other activating agents (like NaOH, $FeCl_3$, $ZnCl_2$, H_3PO_4 etc.) due to intercalation capability of the metallic potassium “K” into any material structure as compared to others which are material specific [14, 15] in developing a better pore network. The activation energy of KOH/C systems is also much lower than most other activating agents [16]. Recently, carbon-containing biomass raw materials (renewable and

waste biomass) have become attractive to scientists in a bid to further enhance material performance, as well as decrease material cost and the amount of toxic elements/waste brought into the environment [17–21].

Similarly, the nature of the electrolyte used in the design of EDLCs is also another contributing factor to their performance. EDLCs working in acidic/basic aqueous electrolytes are known to portray higher ionic conductivity leading to a high specific capacitance (C_s) and small solution resistance (R_s) but unfortunately, they suffer from a restricted operating potential window due to water decomposition which limits their energy density [22, 23].

A much better option in addressing this impediment lies in adopting organic electrolytes; even so their conductivity, stability and handling safety is of major concern. A much promising prospect which addresses all these issues mentioned lies in the use of neutral aqueous electrolytes [24, 25]. Though, they are not as conductive as acidic/basic electrolytes, they still possess a considerably good ionic conductivity as well as extended operating potential window (up to 2 V in some cases) which makes them an ideal choice. Furthermore, they are also environmentally friendly, non-corrosive and can be used in normal atmospheric conditions [25–27]. Albeit there are several reports on the production of AC material from different carbon-containing biomass raw materials for supercapacitor applications with enhanced performance, most of the chemical activation routes employed make use of complicated and lengthy procedures to obtain the final product. This affects the cost, the electrical conductivity and the porosity of the AC material to some extent, due to the extra post-processing steps adopted. Besides, very few similar reports have studied activated carbon from tree bark biomass for electrochemical applications [28, 29].

In the present study, we elucidate a facile synthesis method for the production of porous activated carbon from biomass tree bark (denoted as ACB) shed from an Acacia

auriculiformis tree in South Africa. Optimization of the activated carbon for SC application was carried out using different characterization techniques. Subsequently, the electrochemical performance of the ACB electrode material was analysed in different neutral aqueous electrolytes. The uniqueness of this present work is based on the optimizations of both the amount of the activation agent (KOH pellets) as well as an ideal carbonization temperature used in obtaining the final carbon material from tree bark. In addition, the source of carbon from a dead part of the plant material which adds value to the waste biomass materials forms the basis of this research work. The material electrode is then tested in three different neutral aqueous electrolyte in order to explore the best working electrolyte. The reason for this comprehensive approach was to distinctly establish the best parameters for synthesizing activated carbon from tree bark biomass source applicable to a specific use. Thereafter, the best material electrode was coupled in a symmetric full device and tested. The results obtained from the different characterization techniques in this study provide an interesting and promising trend on account of adopting a particular biomass precursor material as suitable supercapacitor electrodes for energy storage applications.

I. EXPERIMENTAL

Potassium hydroxide (Sigma Aldrich, research grade) was purchased and used as received without further purification. The biomass tree bark was obtained from an Acacia *auriculiformis* tree grown in the University of Pretoria sports ground, Hatfield campus in South Africa and denoted as an Acacia tree bark (ATB) raw material. All other chemicals and gases used in this study were of high purity and analytical grade.

1. Synthesis of Activated carbon from tree bark (ACB) samples

ACB samples were synthesized directly by a KOH-activation process followed by carbonization at three different temperatures (600, 700 and 800 °C) in an attempt to optimize the carbonization process to obtain the porous ACB material. Firstly, the ATB raw material was obtained by crushing large tree bark chunks into smaller pieces using a ball mill crushing machine. Subsequently, the KOH pellets was mixed with ATB raw material with different mass loading in a ratio of 1:1, 2:1 and 3:1 for the KOH and ATB respectively. For example, 10 g of KOH was mixed with 5.0 g of ATB raw material for a ratio of 2:1. The KOH/ATB mixture was left to soak for 48 h before the carbonization step. The mixture was then loaded in a horizontal quartz tube placed in a furnace and ramped up from room temperature to the three different temperatures at 5 °C min^{-1} for each chosen temperature. The carbonization process was carried out for a period of 2 h in each case in the presence of argon and hydrogen gas flow and allowed to cool down naturally to room temperature. Thereafter, the carbonized sample was collected, grinded into a fine powder and sonicated for 30 min in 1 M HCl before rinsing thoroughly with deionized water in order to remove any unreacted KOH and the HCl. The final samples were then filtered, dried at 60 °C and labelled as ACB-X_y where ***X***-denotes the ratio of KOH/ATB and ***y***-indicates the carbonization temperature. The obtained average yield of the ACB samples was 0.55 g for a 5.00 g mass of ATB raw material. A schematic illustrating the entire synthesis route adopted is shown in Fig. 1.

Fig. 1 Schematic illustrating the complete synthesis route of the ACB samples

2. Sample characterization

The surface morphology analysis was carried out using a Zeiss Ultra Plus 55 field emission scanning electron microscope (FE-SEM) operated at 1.0 kV. Transmission electron microscopy (TEM) micrographs and energy dispersive x-ray (EDX) were done using a JEOL-2100F field emission electron microscope operating at an accelerating voltage of 200 kV. SEM/TEM samples were prepared by simply dispersing the ACB powder in ethanol and dropping them onto carbon tape on aluminium stubs and carbon-coated copper grids, respectively.

X-ray photoelectron spectroscopy (XPS) technique was used to further examine the surface chemistry and to quantitatively determine the available active carbon content in the ACB sample. Al-Kα rays was used to irradiate the powder sample surface with survey spectra taken at a pulse energy of 117.5 eV and 0.1 eV step-size. High resolution spectra for the C*1s* and O*1s* sections were obtained at a 23.5 eV pulse energy with a 0.05 eV step-size.

Thermogravimetric analysis (TGA) was also performed on the samples to obtain information on the thermal stability of the materials and the stable sample degassing temperature for surface area analysis. This was carried out with a TA Q600 DSC/TG Instrument which

measures the weight loss over a temperature range (25–1000 °C) in a controlled inert atmosphere (N_2-gas in this case) over time at a ramping rate of 10 °C min^{-1}.

The Brunauer-Emmett-Teller (BET) method was used to determine the surface area and the N_2-absorption/desorption isotherms using a Micromeritics TriStar II 3020 (version 2.00) system at -196 °C in a relative pressure (P/P_o) range of 0.01–1.0 for samples pre-degassed at 140 °C for 18 h. The pore size distribution (PSD) was obtained from the desorption branch of the isotherm using the Barrett-Joyner-Halenda (BJH) method.

Raman spectra were collected from the samples using a WITec Alpha 300R Plus confocal micro-Raman imaging system (WITec GmbH, Germany) with a 532 nm excitation laser set at a power of approximately 5 mW in order to minimize heating effects on the sample. Fourier Transform Infrared (FTIR) spectra were performed using a Bruker Vertex 77v spectrometer within a wavenumber range of 500–3800 cm^{-1}.

3. Electrode sample fabrication and electrochemical characterization

The working electrode was prepared by mixing 80 wt.% of the different activated carbon (ACB-X_y) samples with 10 wt.% of carbon black (CB), 10 wt.% polyvinylidene fluoride (PVdF) binder and 1-methyl-2-pyrrolidinone (NMP) in an agate mortar to form a paste. This was coated onto nickel foam (NF) current collector and dried at 60 °C in an electric oven for 24 h to ensure complete evaporation of the NMP.

All electrochemical tests (ETs) were carried out using a Biologic VMP-300 potentiostat (Knoxville, USA) controlled by an EC-Lab® V10.40 software operated in both a three-electrode and two-electrode configuration in order to determine the electrochemical performance (EP) of the individual material electrode. The three (3) electrode (half-cell device) tests were carried out to get information on the suitable working potential for the

ACB material. Afterwards, the two-electrode (full-cell device) tests were carried out based on the findings in the three electrode tests. This usually aids in understanding the charge storage mechanism occurring within the material electrode for the complete device. To complete the three electrode set-up, a glassy carbon plate and Ag/AgCl (in saturated KCl) served as the counter electrode (CE) and reference electrode (RE), respectively. A swagelok cell system was used for the two electrode tests.

ETs such as cyclic voltammetry (CV), galvanostatic charge-discharge (GCD) or chronopotentiometry (CP), electrochemical impedance spectroscopy (EIS) and cycle-life/stability studies were carried out on the ACB material electrode in three different neutral aqueous electrolytes namely KCl, $NaNO_3$ and Na_2SO_4.

The CV tests were analyzed in a negative operating potential range of -0.80 V to -0.20 V (vs. Ag/AgCl) and in the positive operating potential range of 0.0 to 0.60 V for specific electrolytes at different scan rates ranging from 10 to 100 mV s^{-1}. The CP measurements were also tested at different current densities from 1 to 10 A g^{-1} and the electrochemical impedance spectroscopy (EIS) measurements were performed in the frequency range of 100 kHz-10 mHz. The specific capacitance (C_s) were calculated from the slope of the discharge curve of the CP plot by the relation.[30, 31]

$$C_{\mathrm{s}}\ (\mathrm{F/g}) = \frac{IT_{\mathrm{d}}}{m\Delta V} \qquad \textbf{(1)}$$

where m is the mass of the active material (in g), I is a current applied (A), T_d is the discharge time (s), and ΔV is the potential range (V).

II. RESULTS AND DISCUSSION

Morphological and structural characterization

The SEM micrographs in Fig. 2(a-f) show detailed morphology of the as-prepared ACB sample for a 1:1 mass ratio carbonized between 600–800 °C at low and high magnification. The morphology of the ACB samples carbonized at 800 °C with varying amounts of KOH used in the activation step is shown in Fig. 2(g-i). The presence of a highly porous morphology with interconnecting network is visible in all samples with an open structure containing varying pores dimensions that are clearly visible at higher magnification. The SEM micrographs showed an increase in the range of pore sizes as the carbonization temperature increased and more KOH was used in activation. Numerous smaller-sized pores

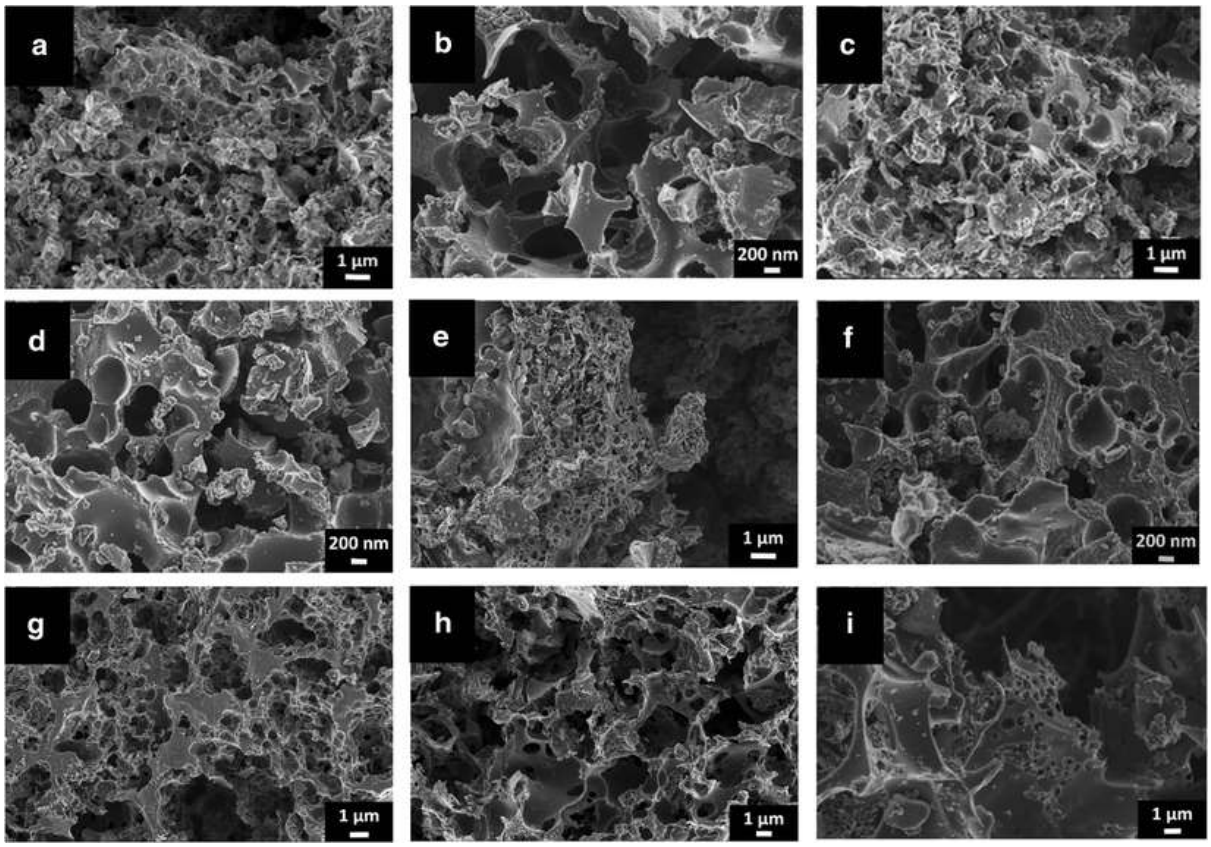

Fig. 2 SEM image of (a,b) ACB-1_{600} at low and higher magnification; (c,d) ACB-1_{700} at low and high magnification; (e,f) ACB-1_{800} at low and high magnification; (g-i) ACB samples with three different KOH/ATB mass ratios carbonized at 800 °C, i.e. ACB-1_{800}, ACB-2_{800}, and ACB-3_{800} respectively

are distinctly visible on the ridges of samples with a higher KOH/ATB ratio (see SEM micrographs in Fig. S1 of the supporting information).

This smaller-sized pores could contribute to the material's charge storage capacity in the penetration of electrolyte ions into the available pore sites which would enhance its electrochemical performance [32]. TEM analysis was also performed as shown in the micrographs in Fig. 3(a-b) which revealed a complete porous carbon architecture even at higher magnification as seen in Fig. 3(b). The existence of these pores are attributed to the KOH activation process adopted in synthesizing the ACB materials [33]. In order to initially confirm the elemental composition of the synthesized material, EDX analysis was performed alongside TEM analysis. The EDX spectrum (Fig. 3c) confirmed the presence of a high

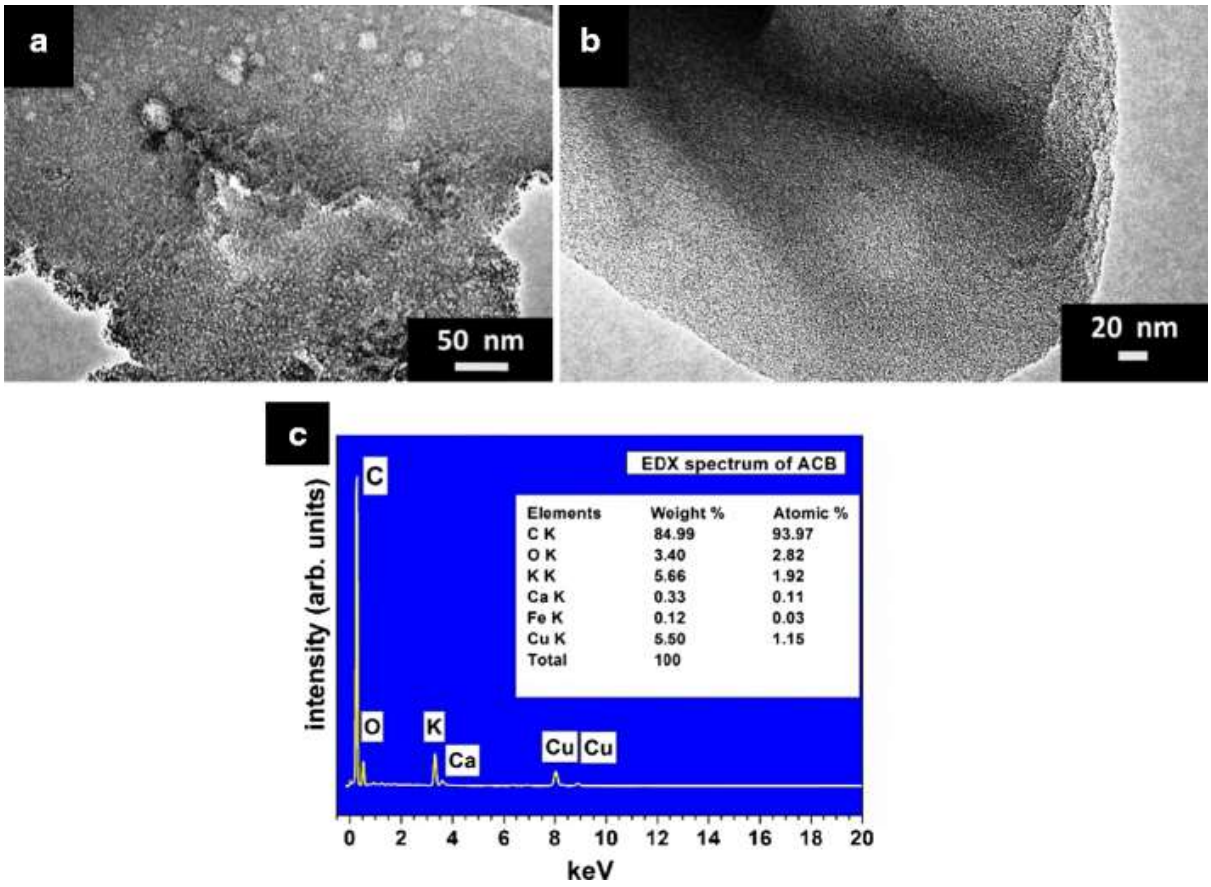

Fig. 3 (a,b) TEM image at low and higher magnification; and (c) EDX spectrum; of ACB sample

amount of carbon content (84.99 wt.%) as compared to oxygen (3.40 wt.%) and potassium (5.66 wt.%) in the sample. Other elements existed in trace amounts with calcium and iron having less than 0.5 wt.%.

To further confirm the presence of high carbon content in the ACB sample, an XPS survey scan for activated carbon samples was carried out (see Fig. 4). Figure 4(a) shows the XPS survey scan for activated carbon which predominantly shows carbon and oxygen. The observed low concentrations of potassium and sulphur could be due to the activation process and the tree plant origin respectively. Fig. 4(b) and 4(c) show the deconvolution of C*1s* and O*1s* core level spectra for activated carbon. In Fig. 4(b), the fitted peaks show a

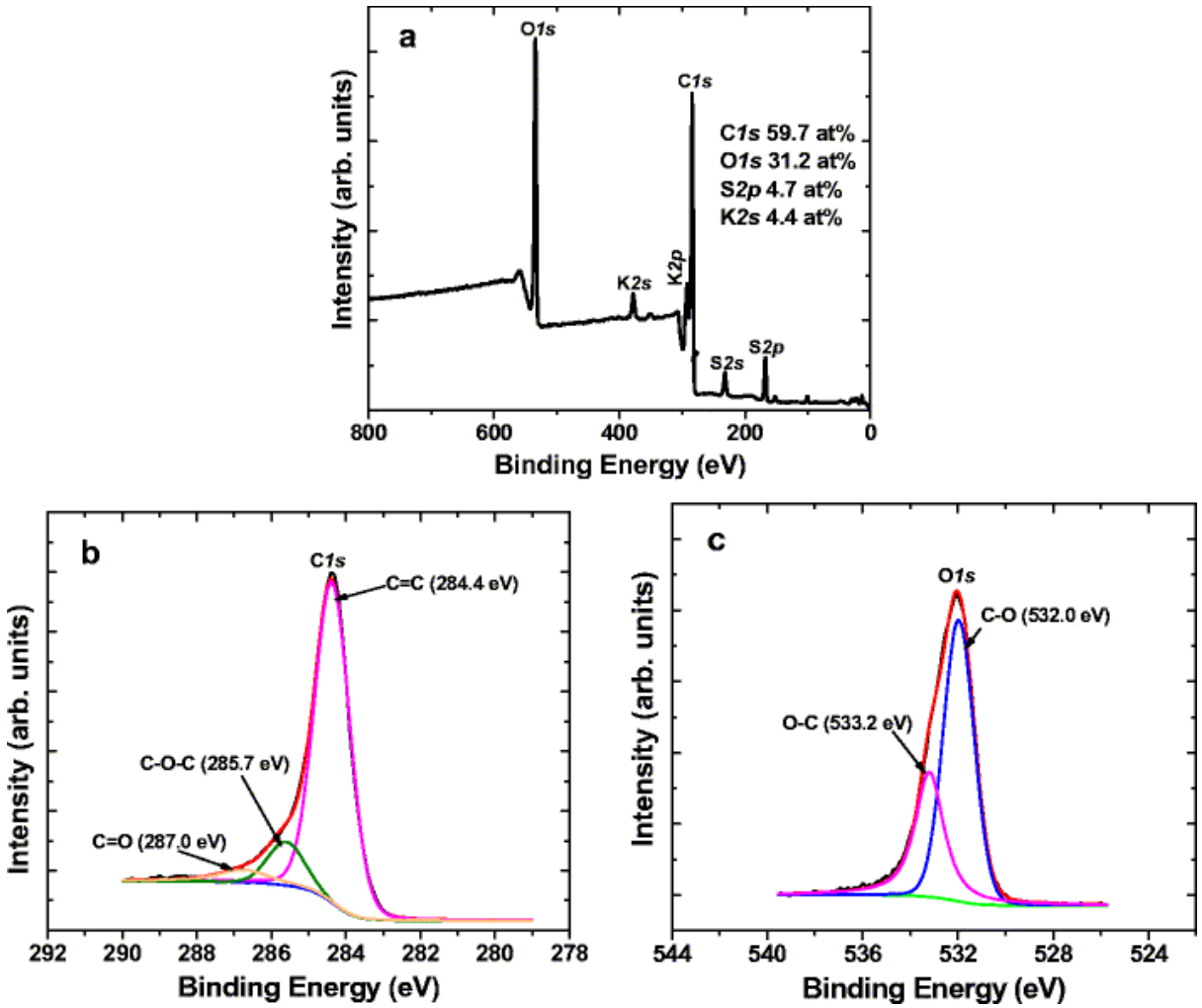

Fig. 4 (a) XPS survey and high-resolution core level spectra of (b) C*1s*, and (c) O*1s* of the activated carbon

dominating intensity at a binding energy of 284.4 eV which corresponds to the graphitic carbon component, C=C. Other peaks at binding energies of 285.7 eV and 287.0 eV were assigned to the oxide components, C–O–C and C=O respectively, which suggests the presence of functional carbon in the sample [34]. Similarly, in Fig. 4(c), the deconvolution of the O*1s* spectrum shows peaks at 532.0 and 533.2 eV assigned to C–O and O–C respectively. This further suggests the presence of functional carbon in the sample [35–37].

TGA/DSC profiles of the ACB samples is reported in Fig. 5a. This revealed two distinct regions of significant weight loss at 85–100 °C and 650–670 °C which correspond to the desorption of physisorbed water and carbon pyrolysis, respectively [28] with 60% of its weight still present at 1000 °C. The profiles obtained with different KOH mass loading carbonized at different temperatures show similar behaviour between room temperature to 1000 °C and as such, a single profile is reported here. These TGA results are also similar to earlier studies on tree bark materials reported by Veeramani and co-workers [28].

Fig. 5(b-c) shows the N_2 adsorption/desorption isotherms and pore size distribution of the ACB sample carbonized between 600 – 800 °C. As observed in Fig. 5(b), all isotherms exhibit a type II isotherm with a type H3 hysteresis loop without any limiting adsorption at high relative pressure (P/P_o). A higher quantity of gas absorbed by the ACB-1_{800} is also recorded, which corresponds to the highest specific surface area (SSA) value of 1017.9 $m^2\ g^{-1}$ for the ACB sample activated at 800 °C.

Peaks are predicted below a pore diameter of 2.0 nm from the BJH PSD curve as well as some observed at about 3.8 nm which corresponds to the presence of micropores and mesopores, respectively. An increase in the pore volume of both micro and mesopores with increasing carbonization temperature is also observed. No direct relationship is observed between the KOH/ATB ratio and the SSA or pore volume although the highest concentration

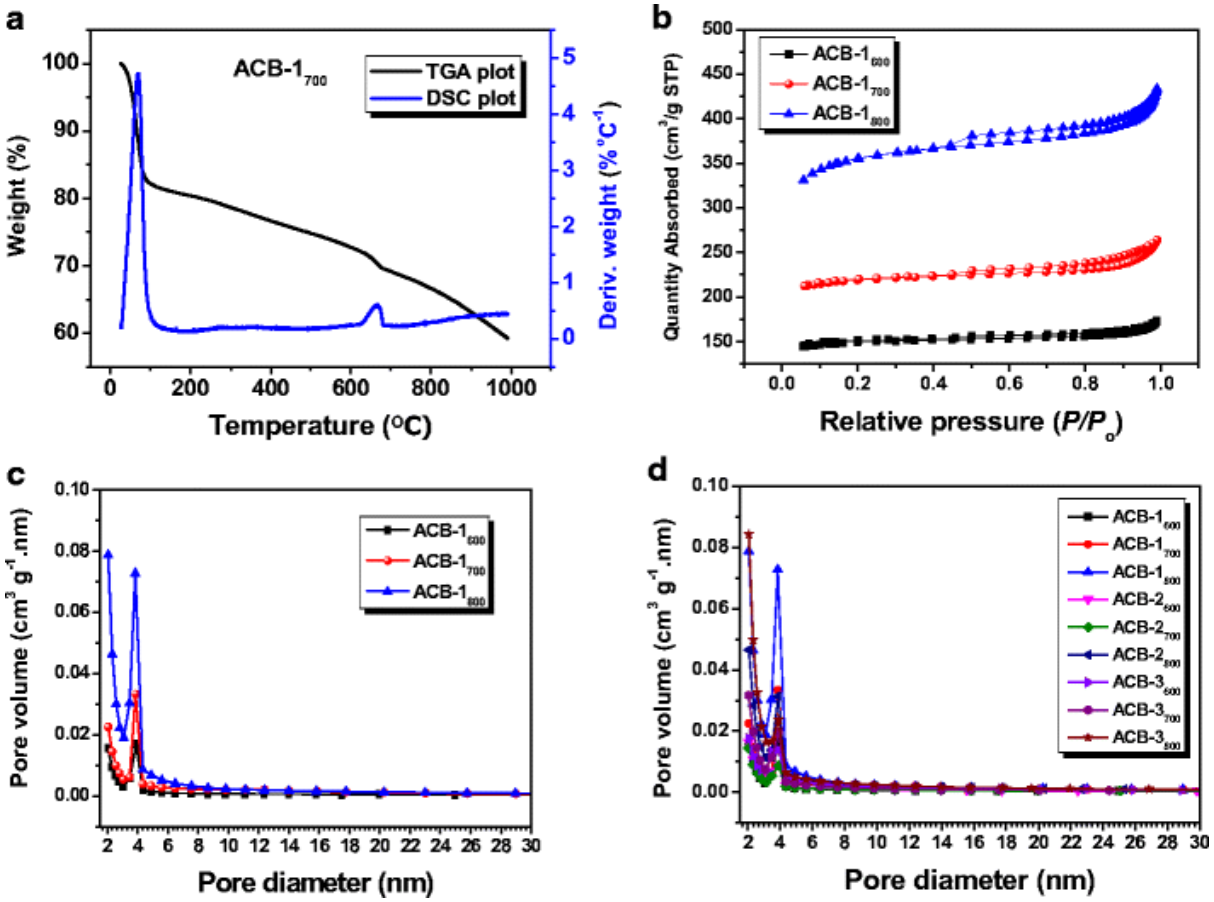

Fig. 5 (a) TGA/DSC plot of the ACB-1_{700} samples (b) N_2 absorption/desorption isotherms and pore size distribution of ACB at 600–800 °C activation temperature (d) pore size distribution of all samples

of micropores is obtained for all samples activated at 800 °C. This also corresponds to the highest SSA values recorded in all the same samples. Table 1 summarizes the surface area properties of all ACB samples with their average PSD. The diverse pore sizes observed provides an efficient charge transport channel and storage site which is essential for high performance electrodes for electrochemical capacitor applications.

Table 1 Specific surface area and porosity data of different ACB samples

Sample (ACB-X_y)	Specific surface area[a] (SSA in $m^2\ g^{-1}$)	Total pore volume[b] (V_{Total}, $cm^3\ g^{-1}$)	Micropore volume[c] (V_{micro}, $cm^3\ g^{-1}$)	Mesopore volume[d] (V_{meso}, $cm^3\ g^{-1}$)	Ave. pore diameter (nm)
ACB-1_{600}	422.9	0.26	0.20	0.06	2.49
ACB-1_{700}	619.5	0.40	0.30	0.10	2.57
ACB-1_{800}	1017.9	0.66	0.43	0.23	2.59
ACB-2_{600}	362.6	0.23	0.18	0.05	2.53
ACB-2_{700}	371.0	0.24	0.18	0.06	2.57
ACB-2_{800}	758.6	0.49	0.34	0.15	2.59
ACB-3_{600}	367.8	0.26	0.17	0.09	2.51
ACB-3_{700}	560.0	0.35	0.26	0.09	2.63
ACB-3_{800}	756.1	0.50	0.29	0.21	2.83

[a]Brunauer–Emmet–Teller (BET) surface areas

[b]Total pore volume obtained from the N_2 uptake at $P/P_0 = 0.99$

[c]pore volume obtained from t-plot analysis

[d]Mesopore volume ($V_{meso} = V_{Total} - V_{micro}$)

Raman spectra of the ACB sample at 600–800 °C carbonization temperatures (Fig. 6a) show no difference in behavior with a comparable D peak (1346 cm^{-1}) to G peak (1587 cm^{-1}) intensity ratio of approximately unity which confirms the presence of a high degree of disordered carbon material [38]. A curve fitting (Lorentzians) of different combinations of the distinct peaks was done for the structural analysis of the ACB samples (see Fig. 6b) which agrees well with the Raman data reported for similar carbonaceous material [25, 39]. From Fig. 6(b), the characteristic G peak arises from the stretching of the C−C bond in graphitic materials and is common to all sp^2 carbon materials [40]. The D1 peak arises from the carbon atoms at the edge and at the edge planes perpendicular to the single carbon-sheets of the bulk graphitic materials [41]. It can be seen that the D1 peak has a higher intensity relative to the G peak which could be due to the activation process which thus contributes to the overall SSA of the ACB material. The D2 peak origin is related to a lattice

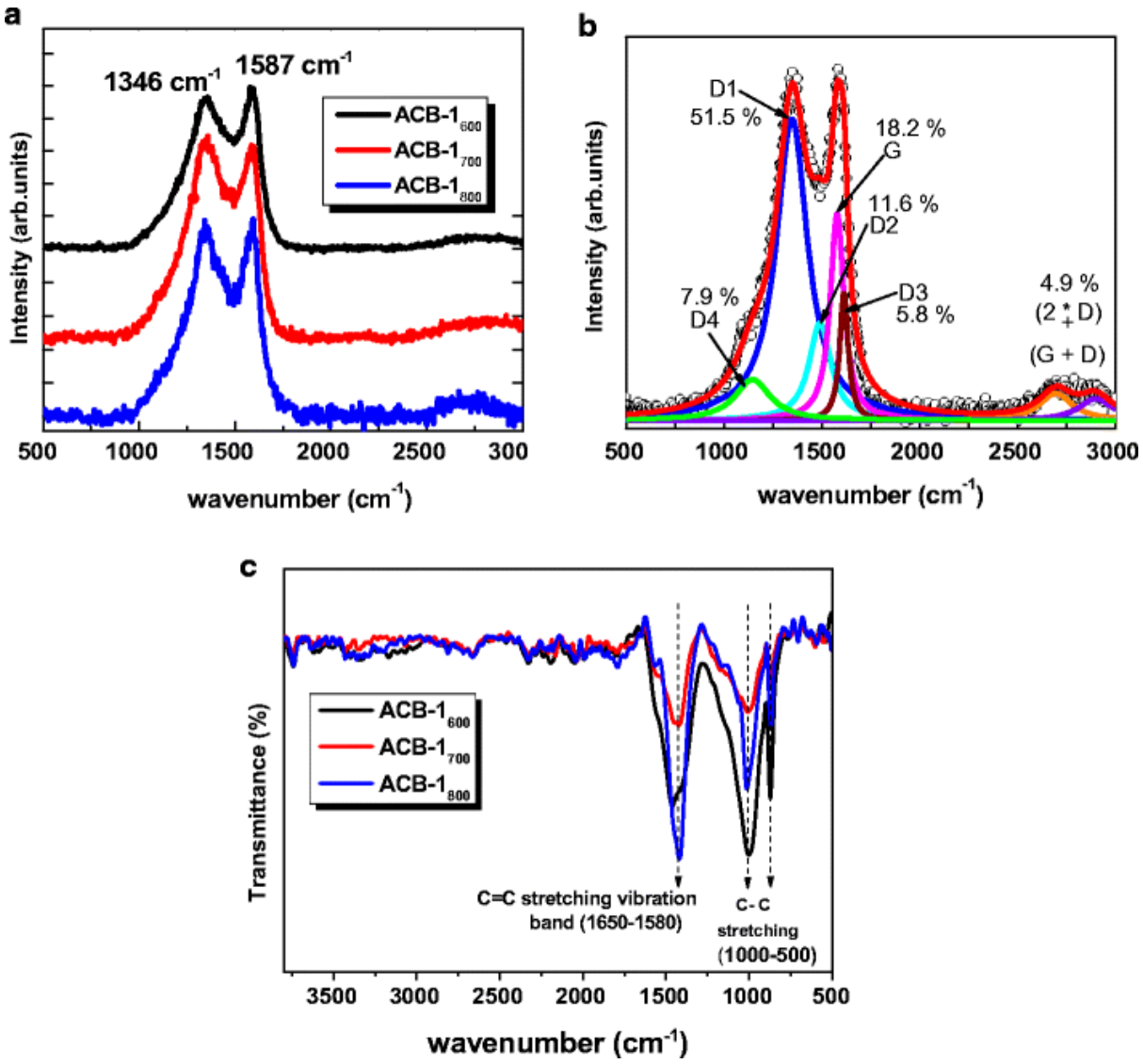

Fig. 6 (a) Raman spectra (λ_0 = 514 nm) of the ACB samples at 600–800 °C activation temperature (b) the corresponding curve fitting (Lorentzians) of different combinations of the Raman peaks for carbonaceous material and the percentages contribution of each peak.(c) FTIR spectra of the ACB samples at 600–800 °C activation temperature

vibration that corresponds to the G peak in the bulk of a carbon material [39]. The D3 peak is related to the amorphous carbon present in interstitial sites in a distorted graphitic lattice of carbonaceous material [42] while the D4 peak exist due to lattice vibrations from sp^2-sp^3 bonds [43, 44].

A significantly lower intensity response of the D2 and D3 peaks gives information on the crystallinity of the material (i.e. D3 contribution arises from the distribution of amorphous carbon in the material). The peaks at ~2700 cm^{-1} and 2900 cm^{-1} are assigned to the (2∗D) overtone and (G+D) combination, respectively [39].

To further confirm the presence of graphitic carbon and investigate the surface functional groups in the synthesized sample, FTIR analysis was also undertaken. The spectra obtained are shown in Fig. 6(c) depicting the C=C stretching vibrational bands at 1560–1650 cm^{-1}. This reveals the aromatization during the activation and carbonization processes [33], aiding in enhancing the ACB sample conductivity [45]. The bands observed between 500–1000 cm^{-1} can be assigned to the –C–C– stretching vibrations after carbonization [36, 46].

Electrochemical characterization

Carbonization temperature has a significant effect on the electrochemical behaviour of supercapacitor electrode materials [47]. Fig. 7(a-c) shows the cyclic voltammogram (CV) plots at a scan rate of 20 mV s^{-1} for the ACB-1 material activated between 600–800 °C in different neutral electrolytes. The CV plots show ideal capacitive behavior with a rectangular shape for the sample tested in all three aqueous electrolyte indicating that the ACB samples exhibited a good electric double layer storage mechanism. Although a slightly distorted shape is seen in samples tested in 1 M $NaNO_3$ which indicates a kinetic process limitation of ion transfer [45].

Fig. 7(d) also depicts the reversible operating capability of the ACB electrode material in 1 M Na_2SO_4 aqueous electrolyte to elucidate its possibility to work in both positive and negative potential which increases its flexibility in application as an EDLC electrode material. However, it is observed that a higher current response is attained from scanning in a negative potential with a higher operating potential window. The reason for the good EDLC

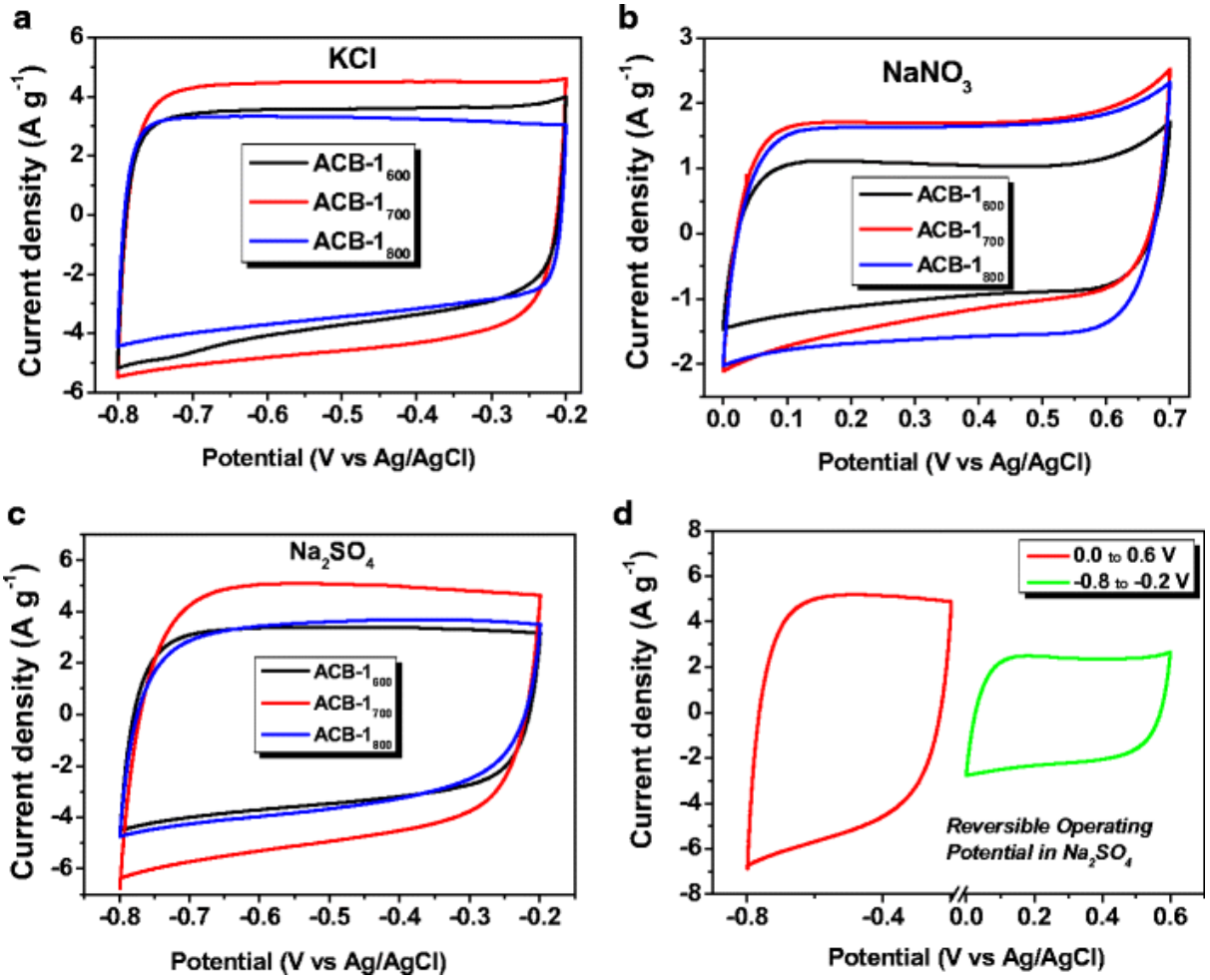

Fig. 7 (a-c) CV plots of ACB-1 sample in different electrolytes at different activation temperatures (d) CV plot showing reversibility of ACB-1_{700} material electrode in Na_2SO_4 aqueous electrolyte

response in Na_2SO_4 is attributed to its unique properties such as the hydration sphere radius, ionic mobility, the electrolyte pH-value, conductivity etc. as reported in earlier studies [48–50] on activated carbon materials for both alkaline and neutral electrolytes.

In addition, all CV plots of the sample electrodes carbonized at 700 °C show the highest current response, indicating superior capacitance and an optimum carbonization temperature of 700 °C for the ACB material. To further confirm this assertion made based on the current response in relation to capacitance, the galvanostatic charge-discharge (GCD) plots at a current density of 1 A g^{-1} are also presented in Fig. S2(a-c) of the supporting

information. It can be observed that the GCD plots obtained are symmetrically triangular with the longer discharge times (T_D) recorded for the ACB sample carbonized at 700 °C in all electrolytes. Fig. S2(d) also shows the comparison of stability of the ACB-1_{700} material tested in different electrolytes. The Na_2SO_4 electrolyte provides the most stable operating medium with the highest coulombic efficiency of 99.8% over 2000 continuous charge-discharge cycles at a constant current density. There was a slight decrease in coulombic efficiency (99.5%) observed when the sample was cycled in the KCl electrolyte and a major coulombic efficiency decrease from the $NaNO_3$ electrolyte (95.9%) after 2000 cycles. Based on the CV plots reported in Fig. 7 and the electrolyte stability during cycling, the 1 M Na_2SO_4 electrolyte was selected as the best electrolyte to test the ACB material in addition to its exhibition of a close to ideal EDLC behavior, good current response, stability over continuous cycling and the ability for the ACB material operate in both positive and negative potentials.

Fig. 8(a) and 8(b) show the detailed CV and GCD tests performed on the ACB-1_{700} electrode material at various scan rate and current densities respectively. The CV plots show a characteristic electrochemical double layer capacitor (EDLC) behaviour which indicates its polarizable and porous capability of the material [36]. However, as scan rate increases up to 100 mV s^{-1}, the CVs begins to show some form of distortion (resistive CV shape) due to increased ohmic behaviour which leads to a capacitance deterioration [51]. This is confirmed with the reduced discharge times recorded in the corresponding GCD curves as the current density increases from 1 – 10 A g^{-1}. Nonetheless, the capacitive double layer signature of the electrode is still present, indicating the high power ability of the ACB electrode material.

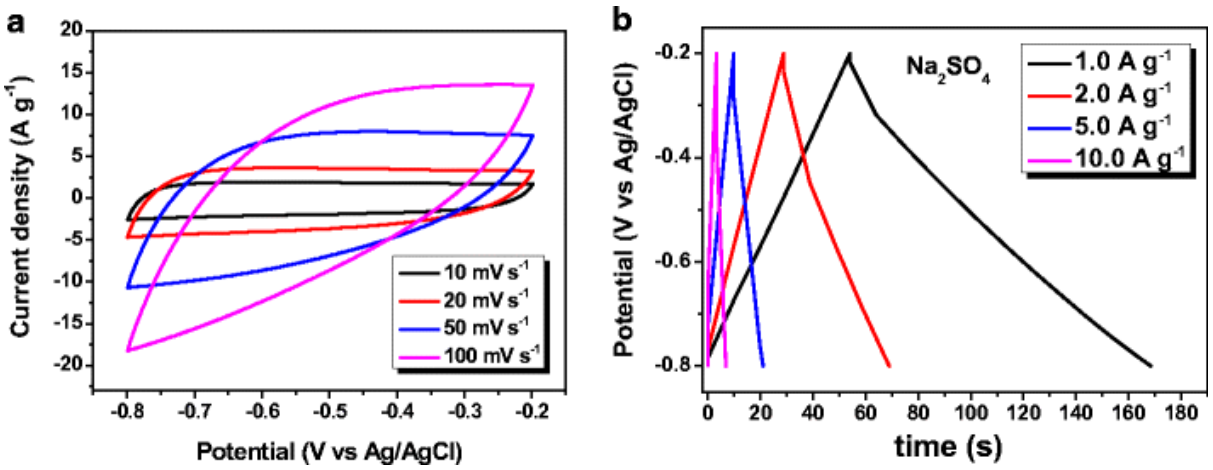

Fig. 8 Detailed (a) CV and (b) GCD plots of the ACB-1_{700} sample in Na_2SO_4 electrolyte at different scan rates and current densities respectively

Electrochemical impedance analysis results are reported in Fig. S3 (a-c) with the Nyquist plots for the ACB-1 material carbonized between 600–800 °C in Na_2SO_4 electrolyte (as shown in Fig. S3(a)). All samples at different temperatures show the features of a typical porous carbon electrodes with an intercept and characteristic semicircle on the *Z*'-axis, Warburg region from the high to mid-frequency region. At low frequencies, the plots appear to have a nearly ideal capacitive behavior with a slight tilt of the vertical line which is attributed to the leakage resistance. In the high to mid-frequency region, the intercept of the semicircle with the *Z*'-axis in the high frequency end corresponds to the solution resistance (R_s) which is composed of the resistance of both the electrolyte, contact resistance at the active material/current collector interface and the internal resistance of the electrode [52].

The R_s values for different materials carbonized at different temperatures are indicated in the inset to Fig. S3(a). Fig. S3(b) represents the Nyquist plot of the ACB-1_{700} fitted by a modified Randles circuit [53] that fits the experimental data using an EIS data fitting software (ZFIT) which applies the complex nonlinear least-squares (CNLS) method [54]. The

plot shows a perfect fit with the experimental data of the fitting parameters. From the circuit diagram obtained, the equivalent series resistance, R_S is in series with the constant phase element, *Q* and an inductor. At high frequency, an inductance (*L*) is observed which has been observed as an EDLC type behavior when materials are tested over a wide range of frequency. This has been described by simulation models to denote a stray inductance within the electrode material which could be influenced by its geometry [55, 56]. A charge transfer resistance R_{CT} models the small semi-circular arc in the high to mid-frequency region and a constant phase element, *Q* which is responsible for the ideal capacitance are connected in parallel to each other. The associated Bode plot for the ACB-1_{700} is also shown in Fig. S3(c) showing a phase angle of -81.4° which is close to ideal capacitors with -90° phase angle.

A summary of the electrochemical performance characteristics; the specific capacitance (C_s) at a current density of 1 A g^{-1} (calculated using equation 1) in the three electrolytes, the corresponding solution resistance (R_s) values of the ACB electrode material activated for all three carbonization temperatures and KOH/ATB mass loading ratios is reported in Table 2. From the data in the table, it is seen that the C_s-values initially increase with increasing carbonization temperature from 600–700 °C in all electrolytes, but decrease as the temperature further increases to 800 °C. This is linked to average pore size enlargement effect shown in the average pore diameter values reported from the BET results in Table 1.

Higher carbonization temperatures possibly led to a breakdown of the porous structure suitable for efficient transport of electrolyte ions for efficient charge storage even with higher SSA. A similar trend was exhibited for all three sets of ACB samples and has also been explained in another recently published study [45] on KOH-activated porous carbons. In

general, the ACB-1_{700} exhibited the best electrochemical response in terms of average calculated specific capacitance values in all three electrolytes.

A specific capacitance of 247, 79 and 191 F g^{-1} was obtained for the ACB-1_{700} material in KCl, $NaNo_3$ and Na_2SO_4 electrolytes respectively. These values are comparable with other related studies involving the synthesis of activated carbon from plant biomass for supercapacitor applications [57–59]. Although the KCl electrolyte provides a higher overall C_s-value, (which is expected based on its lower R_s values, see Table 2), the stability of the electrolyte for practical full device applications makes the Na_2SO_4 a better option in our study.

Table 2 Summary of electrochemical performance values for the different ACB samples adopted as electrode materials for supercapacitor application

Sample electrode (ACB-X_y)	**KCl (aq) specific capacitance (C_s in F g^{-1})**	**$NaNO_3$ (aq) specific capacitance (C_s in F g^{-1})**	**Na_2SO_4 (aq) specific capacitance (C_s in F g^{-1})**	**KCl (aq) solution resistance (R_s in Ω)**	**$NaNO_3$ (aq) solution resistance (R_s in Ω)**	**Na_2SO_4 (aq) solution resistance (R_s in Ω)**
ACB-1_{600}	192	64	151	1.65	5.41	2.05
ACB-1_{700}	*247*	*79*	*191*	*1.46*	*4.12*	*2.73*
ACB-1_{800}	175	76	148	1.55	5.47	2.27
ACB-2_{600}	150	60	95	1.71	5.14	2.16
ACB-2_{700}	246	76	157	1.48	4.84	2.43
ACB-2_{800}	127	59	128	1.71	6.98	2.53
ACB-3_{600}	127	39	127	2.06	5.03	2.06
ACB-3_{700}	150	63	160	1.34	5.68	2.47
ACB-3_{800}	138	59	125	1.70	6.76	2.64

The observed trend has also been explained in earlier reports by Cheng Zhong *et al*. [50] which considered studies on electrolyte materials and compositions for electrochemical supercapacitors. Based on the different ion properties summarized, it can be seen that the K^+ hydrated ion size and ionic conductivity (3.31 Å/73.5 S cm^2 mol^{-1}) is smaller compared to the Na^+ hydrated ion size and ionic conductivity (3.58 Å/50.11 S cm^2 mol^{-1}). However, we also consider the ionic conductivity and hydrated ion size of the SO_4^{2-} anion (160.0 S cm^2 mol^{-1} and 3.79 Å) compared with Cl^- ion (76.31 S cm^2 mol^{-1}) respectively.

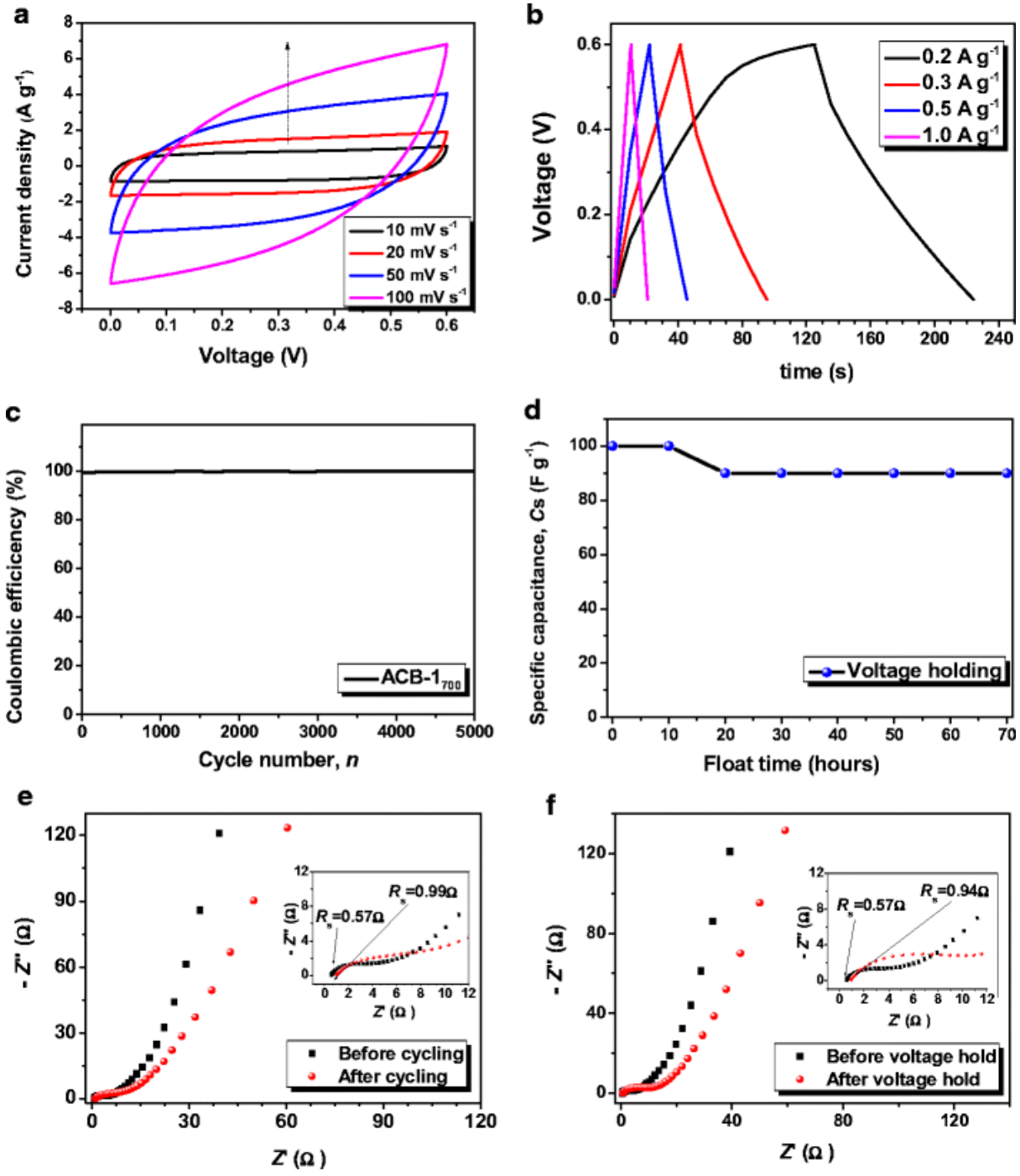

Fig. 9 Electrochemical test of the full ACB device: (a) CV curves at varying scan rates; (b) galvanostatic charge/discharge curves at different current densities (c) cyclic stability showing the device coulombic efficiency for a symmetric device with ACB-1_{700} material; (d) plot showing the capacitance degradation with voltage holding for 70 h; Nyquist plots of ACB/ACB symmetric cell before and after (e) cycling (f) voltage holding

The ACB-1_{700} material was then coupled into a two-electrode symmetric device set-up in order to test the electrochemical behavior of a complete cell. Fig. 9 shows the electrochemical performance results of the coupled ACB//ACB symmetric supercapacitor tested in a 1 M Na_2SO_4 electrolyte. Fig. 9(a) shows the CV plots at different scan rates from 10–100 mV s^{-1} in a 0.60 V operating voltage window. A close to ideal rectangular shape is also observed in the CV curves which signifies pure capacitive behavior with a distortion to the shape appearing at increased scan rates due to the emergence of ohmic processes discussed earlier [60]. Likewise, the galvanostatic charge-discharge curves (Fig. 9(b)) depicts a triangular shape even as the current density increases. This linear form of the charge-discharge profile confirms the reversible ion adsorption/desorption at the electrode/electrolyte interface.

A C_S value of 114 F g^{-1} was recorded for the symmetric cell at a 0.3 A g^{-1} current density. This value is reasonable and comparable with similar reports on activated carbon from plant materials [21, 61, 62]. It is worthy to point out the difficulty in adequately comparing the performance of supercapacitor electrodes based on plant biomass materials due to varying synthesis routes, electrode material parameters and testing conditions. Nevertheless, the results obtained here, demonstrate considerable scientific contribution to the electrochemical energy storage.

The stability of the symmetric cell was initially examined by analysing the coulombic efficiency drop over 5000 continuous charge-discharge cycles at a current density of 5 A g^{-1} (see Fig. 9(c)). Thereafter, the traditional continuous charge-discharge cycles was complemented with a floating test which involved subjecting the full cell to a voltage holding [63] for an extended period of time (approx. 3 days) and the results are illustrated in Fig. 9(d). A maximum coulombic efficiency value of 100% was retained even after

continuous cycling for 5000 cycles. A decrease of ~10% of the total specific capacitance value was initially observed after 20 h of holding with no further drop in the capacitance observed even up to 70 h as seen in Fig. 9(d). This good electrochemical performance is credited to the micropore/mesopore distribution within the ACB material which provides the relevant pore sites accessible to electrolyte ions along with short diffusion paths supporting fast ions transport during the lengthy charge-discharge process.

Simply put, the high ionic conductivity ensures easier ion-transport within the electrolyte to enhance charge storage in the porous sites, thereby improving the overall electrochemical performance of the electrode material and the entire device. Fig. 9(e) and 9(f) show the Nyquist plots before and after the device was subjected to both cycling and voltage holding. An initial negligible increase in the R_s value is recorded from the cycling process from an initial value of 0.57 Ω to 0.99 Ω and 0.94 Ω for both after the cycling and holding process respectively [31, 64]. This has been studied extensively and is elucidated to be due to the formation of inactive sites caused by the partial collapse of the carbon material structure during the continuous cycling. However, the R_s value is seen to later improve when the device is subjected to voltage holding for 70 h. In both cases, an insignificant amount of degradation occurs during the stability tests.

These results show the long term electrochemical stability and high degree of charge-discharge reversibility. Thus, these combined results show the suitability of the ACB electrode for practical electrochemical capacitor applications due to all the promising characteristics demonstrated thus far.

III. CONCLUSION

In summary, a facile activation and carbonization technique was adopted and optimized in synthesizing highly porous carbons from plant biomass (Acacia *auriculiformis* tree) by varying the carbonization temperature, KOH mass loading with the ATB and neutral electrolyte used. The optimization was carried out to indicate the necessity to establish the best parameters for synthesizing activated carbon from different biomass sources for various electrochemical application. The as-synthesized samples (denoted as ACB) possessed a large specific surface area up to 1017.9 $m^2\ g^{-1}$ and total pore volume of 0.66 $cm^3\ g^{-1}$ consisting mainly mesopores and micropores beneficial for ion transport and charge storage.

The SEM and TEM micrographs revealed a porous structure with varying distribution of pore sizes necessary for ion penetration from the electrolyte in order to improve electrochemical performance. The EDX, XPS and Raman spectroscopy results confirms the presence of a high quality carbon containing material with carbon functionalities.

As such, when tested as electrodes for supercapacitor, the porous activated carbons exhibited the best prospective electrochemical properties in the Na_2SO_4 electrolyte operating reversibly in both positive and negative potential range. Overall, the combination of the sample activated at 700 °C in Na_2SO_4 was chosen with a C_S value of 191 F g^{-1} at a 1 A g^{-1} current density and 99.8% coulombic efficiency. This demonstrates a good rate capability attributed to the ionic properties of the electrolyte ions which provide little resistance to mobility. A complete symmetric cell fabricated afterwards, exhibited a C_S value of 114 F g^{-1} with an excellent coulombic efficiency of 100% and a negligible loss in capacitance for a floating time of 70 h. These results contributes to the field of energy storage by exploring a

low cost plant biomass raw material as a green (environmentally friendly) and non-toxic carbon source for potential EDLC materials for energy storage.

IV. ACKNOWLEDGEMENT

The authors will like to specially thank Isbe VanDerWesthuizen for the results obtained from the TGA analysis. This work is based on the research supported by the South African Research Chairs Initiative of the Department of Science and Technology, Republic of South Africa and National Research Foundation of South Africa (Grant no.97994). Any opinion, finding and conclusion or recommendation expressed in this material is that of the author(s) and the NRF does not accept any liability in this regard. D. Momodu and F. Barzegar will like to acknowledge financial support from the University of Pretoria for their postdoctoral study.

References

1. Sun Y, Wu Q, Shi G (2011) Graphene based new energy materials. Energy Environ Sci 4:1113

2. Ghoniem AF (2011) Needs, resources and climate change: Clean and efficient conversion technologies. Prog Energy Combust Sci 37:15–51

3. Patel MR (2005) Wind and solar power systems: design, analysis, and operation. CRC press

4. Miller JR, Outlaw RA, Holloway BC (2010) Graphene double-layer capacitor with ac line-filtering performance. Science 329:1637–9

5. Chmiola J, Largeot C, Taberna PL, Simon P, Gogotsi Y (2010) Monolithic carbide-derived carbon films for micro-supercapacitors. Science 328:480–3

6. Wei L, Sevilla M, Fuertes AB, Mokaya R, Yushin G (2012) Polypyrrole-Derived Activated Carbons for High-Performance Electrical Double-Layer Capacitors with Ionic Liquid Electrolyte. Adv Funct Mater 22:827–834

7. Daffos B, Taberna PL, Gogotsi Y, Simon P (2010) Recent advances in understanding the capacitive storage in microporous carbons. Fuel Cells 10:819–824

8. Simon P, Gogotsi Y (2013) Capacitive Energy Storage in Nanostructured Carbon-Electrolyte Systems. Acc Chem Res 46:1094–1103

9. Miller JR, Burke AF (2008) Electrochemical capacitors: Challenges and opportunities for real-world applications. Electrochem Soc 17:53–57

10. Béguin F, Presser V, Balducci A, Frackowiak E (2014) Carbons and electrolytes for advanced supercapacitors. Adv Mater 26:2219–51, 2283

11. Conway BE, Birss V, Wojtowicz J (1997) The role and utilization of pseudocapacitance for energy storage by supercapacitors. J Power Sources 66:1–14

12. Wei L, Yushin G (2012) Nanostructured activated carbons from natural precursors for electrical double layer capacitors. Nano Energy 1:552–565

13. Simon P, Gogotsi Y (2008) Materials for electrochemical capacitors. Nat Mater 7:845–854

14. Lillo-Ródenas MA, Cazorla-Amorós D, Linares-Solano A, (2005) KOH and NaOH activation mechanisms of multiwalled carbon nanotubes with different structural organisation. Carbon 43:786–795

15. Chowdhury ZZ, Hamid SBA, Das R, Hasan MR, Zain SM, Khalid K, and Uddin MN (2013) Preparation of Carbonaceous Adsorbents from Lignocellulosic Biomass and Their Use in Removal of Contaminants from Aqueous Solution. BioResources 8:6523–6555

16. Lillo-Ródenas MA, Cazorla-Amorós D, Linares-Solano A (2003) Understanding chemical reactions between carbons and NaOH and KOH: An insight into the chemical activation mechanism. Carbon 41:267–275

17. Yang K, Peng J, Srinivasakannan C, Zhang H, Xia H, Duan X (2010) Preparation of high surface area activated carbon from coconut shells using microwave heating. Bioresour Technol 101:6163–9

18. Zhi M, Yang F, Meng F, Li M, Manivannan A, Wu NN (2014) Effects of Pore Structure on Performance of An Activated-Carbon Supercapacitor Electrode Recycled from Scrap Waste Tire Effects of Pore Structure on Performance of An Activated-Carbon Supercapacitor Electrode Recycled from Scrap Waste Tire. ACS Sustain Chem Eng 2:1592−1598

19. Wei L, Yushin G (2011) Electrical double layer capacitors with activated sucrose-derived carbon electrodes. Carbon 49:4830–4838

20. Stavropoulos GG, Zabaniotou AA (2009) Minimizing activated carbons production cost. Fuel Process Technol 90:952–957

21. Divyashree A, Gurumurthy H (2015) Activated carbon nanospheres derived from bio-waste materials for supercapacitor applications – a review. RSC Adv 5:88339–88352

22. Abbas Q, Pajak D, Frackowiak E, Beguin F (2014) Effect of binder on the performance of carbon/carbon symmetric capacitors in salt aqueous electrolyte. Electrochim Acta 140:132–138

23. Hong MS, Lee SH, Kim SW (2002) Use of KCl Aqueous Electrolyte for 2 V Manganese Oxide/Activated Carbon Hybrid Capacitor. Electrochem Solid-State Lett 5:A227

24. Bichat MP, Raymundo-Piñero E, Béguin F (2010) High voltage supercapacitor built with seaweed carbons in neutral aqueous electrolyte. Carbon 48:4351–4361

25. Zhang H, Zhang L, Chen J, Su H, Liu F, Yang W (2016) One-step synthesis of hierarchically porous carbons for high-performance electric double layer supercapacitors. J Power Sources 315:120–126

26. Wang JG, Yang Y, Huang ZH, Kang F (2013) A high-performance asymmetric supercapacitor based on carbon and carbon–MnO_2 nanofiber electrodes. Carbon 61:190–199

27. Dyatkin B, Presser V, Heon M, Lukatskaya MR, Beidaghi M, Gogotsi Y (2013) Development of a green supercapacitor composed entirely of environmentally friendly materials. ChemSusChem 6:2269–80

28. Veeramani V, Madhu R, Chen SM, Veerakumar P, Syu JJ, Liu SB (2015) Cajeput tree bark derived activated carbon for the practical electrochemical detection of vanillin. New J Chem 39:9109–9115

29. Koutcheiko S, Vorontsov V (2013) Activated carbon derived from wood biochar and its application in supercapacitors. J Biobased Mater Bioenergy 7:733–740

30. Wang J, Song Y, Li Z, Liu Q, Zhou J, Jing X, Zhang M, Jiang Z (2010) In Situ Ni/Al Layered Double Hydroxide and Its Electrochemical Capacitance Performance. Energy & Fuels 24:6463–6467

31. Yang W, Gao Z, Wang J, Ma J, Zhang M, Liu L (2013) Solvothermal one-step synthesis of Ni-Al layered double hydroxide/carbon nanotube/reduced graphene oxide sheet ternary nanocomposite with ultrahigh capacitance for supercapacitors. ACS Appl Mater Interfaces 5:5443–5454

32. Barzegar F, Bello A, Fashedemi OO, Dangbegnon JK, Momodu DY, Taghizadeh F, Manyala N (2015) Synthesis of 3D porous carbon based on cheap polymers and graphene foam for high-performance electrochemical capacitors. Electrochim Acta 180:442–450.

33. Sun H, He W, Zong C, Lu L (2013) Template-free synthesis of renewable macroporous carbon via yeast cells for high-performance supercapacitor electrode materials. ACS Appl Mater Interfaces 5:2261–2268

34. Wei L, Tian K, Jin Y, Zhang X, Guo X (2016) Three-dimensional porous hollow microspheres of activated carbon for high-performance electrical double-layer capacitors. Microporous Mesoporous Mater 227:210–218

35. Li H, Kang Z, Liu Y, Lee ST (2012) Carbon nanodots: synthesis, properties and applications. J Mater Chem 22:24230

36. Bello A, Manyala N, Barzegar F, Khaleed AA, Momodu DY, Dangbegnon JK (2016) Renewable pine cone biomass derived carbon materials for supercapacitor application. RSC Adv 6:1800–1809

37. Luo QP, Huang L, Gao X, Cheng Y, Yao B, Hu Z, Wan J, Xiao X, Zhou J (2015) Activated carbon derived from melaleuca barks for outstanding high-rate supercapacitors. Nanotechnology 26:304004

38. Mao Y, Duan H, Xu B, Zhang L, Hu Y, Zhao C, Wang Z, Chen L, Yang Y (2012) Lithium storage in nitrogen-rich mesoporous carbon materials. Energy Environ Sci 5:7950

39. Sadezky A, Muckenhuber H, Grothe H, Niessner R, Poschl U (2005) Raman microspectroscopy of soot and related carbonaceous materials: Spectral analysis and structural information. Carbon 43:1731–1742

40. Malard LMM, Pimenta MAA, Dresselhaus G, Dresselhaus MSS (2009) Raman spectroscopy in graphene. Phys Rep 473:51–87

41. Wang Y, Alsmeyer DC, McCreery RL (1990) Raman Spectroscopy of Carbon Materials: Structural Basis of Observed Spectra. Chem Mater 2:557–563

42. Jawhari T, Roid A, Casado J (1995) Raman spectroscopic characterization of some commercially available carbon black materials. Carbon 33:1561–1565

43. Sze SK, Siddique N, Sloan JJ, Escribano R (2001) Raman spectroscopic characterization of carbonaceous aerosols. Atmos Environ 35:561–568

44. Dippel B, Jander H, Heintzenberg J (1999) NIR FT Raman spectroscopic study of flame soot. Phys Chem Chem Phys 1:4707–4712

45. Yao L, Yang G, Han P, Tang Z, Yang J (2016) Three-dimensional beehive-like hierarchical porous polyacrylonitrile-based carbons as a high performance supercapacitor electrodes. J Power Sources 315:209–217

46. Ofomaja AE, Naidoo EB (2011) Biosorption of copper from aqueous solution by chemically activated pine cone: A kinetic study. Chem Eng J 175:260–270

47. Xie K, Qin X, Wang X, Wang Y, Tao H, Wu Q, Yang L, Hu Z (2012) Carbon nanocages as supercapacitor electrode materials. Adv Mater 24:347–352

48. Barzegar F, Momodu DY, Fashedemi OO, Bello A, Dangbegnon JK, Manyala N (2015) Investigation of different aqueous electrolytes on the electrochemical performance of activated carbon-based supercapacitors. RSC Adv 5:107482–107487

49. Toupin M, Bélanger D, Hill IR, Quinn D (2005) Performance of experimental carbon blacks in aqueous supercapacitors. J Power Sources 140:203–210.

50. Zhong C, Deng Y, Hu W, Qiao J, Zhang L, Zhang J (2015) A review of electrolyte materials and compositions for electrochemical supercapacitors. Chem Soc Rev 44:7484–7539

51. Zhang C, Hatzell KB, Boota M, Dyatkin B, Beidaghi M, Lng D, Qiao W, Kumbur EC, Gogotsi Y (2014) Highly porous carbon spheres for electrochemical capacitors and capacitive flowable suspension electrodes. Carbon 77:155–164

52. Fan Z, Yan J, Wei T, Zhi L, Ning G, Li T, Wei F (2011) Asymmetric Supercapacitors Based on Graphene/MnO2 and Activated Carbon Nanofiber Electrodes with High Power and Energy Density. Adv Funct Mater 21:2366–2375

53. Randles JEB (1947) Kinetics of rapid electrode reactions. Discuss Faraday Soc 1:11–19.

54. Conway B. (1999) Electrochemical supercapacitors: Scientific fundamentals and technological applications. Kluwer Academic Publishers, Plenum Press:, New York

55. Bohlen O, Kowal J, Sauer DU (2007) Ageing behaviour of electrochemical double layer capacitors. Part I. Experimental study and ageing model. J Power Sources 172:468–475

56. Bohlen O, Kowal J, Dirk Uwe Sauer (2007) Ageing behaviour of electrochemical double layer capacitors. Part II. Lifetime simulation model for dynamic applications. J Power Sources 173:626–632

57. Saha D, Li Y, Bi Z, Chen J, Keum JK, Hensley DK, Grappe HA, Meyer HM, Dai S, Paranthaman MP, Naskar AK (2014) Studies on Supercapacitor Electrode Material from Activated Lignin- Derived Mesoporous Carbon. Langmuir 30:900–910

58. Volperts A, Dobele G, Ozolins J, Mironova-Ulmane N (2015) Synthesis and Application of Nanoporous Activated Carbon in Supercapacitors. Mater Sci Appl Chem 31:16

59. Ferrero GA, Fuertes AB, Sevilla M (2015) From Soybean residue to advanced supercapacitors. Sci Rep 5:16618

60. Wu ZS, Ren W, Wang DW, Li F, Liu B, Cheng HM (2010) High-energy MnO2 nanowire/graphene and graphene asymmetric electrochemical capacitors. ACS Nano 4:5835–5842

61. Wu FC, Tseng RL, Hu CC, Wang CC (2005) Effects of pore structure and electrolyte on the capacitive characteristics of steam- and KOH-activated carbons for supercapacitors. J Power Sources 144:302–309

62. Syarif N, Tribidasari I, Wibowo W (2013) Binder-less activated carbon electrode from gelam wood for use in supercapacitors. J Electrochem Sci Eng 3:37–45

63. Ratajczak P, Jurewicz K, Béguin F (2014) Factors contributing to ageing of high voltage carbon/carbon supercapacitors in salt aqueous electrolyte. J Appl Electrochem 44:475–480

64. Zhang L, Wang J, Zhu J, Zhang X, San Hui K, Hui KN (2013) 3D porous layered double hydroxides grown on graphene as advanced electrochemical pseudocapacitor materials. J Mater Chem A 1:904